SCIENCE CHINA
Chemistry

•ARTICLES•

August 2022 Vol.65 No.8: 1661–1669
https://doi.org/10.1007/s11426-022-1288-0

Hierarchical ZrO_2@N-doped carbon nano-networks anchored ultrafine Pd nanoparticles for highly efficient catalytic hydrogenation

Chun Pu[1†], Rui-Dong Li[1†], Gang-Gang Chang[1*], Min-Jie Chen[1], Yao Yao[1], Jun-Sheng Li[1], Bo Zhao[2], Lu Wu[3], Yue-Xing Zhang[3*] & Xiao-Yu Yang[1*]

[1]*School of Chemistry, Chemical Engineering and Life Science & State Key Laboratory of Advanced Technology for Materials Synthesis and Processing, Wuhan University of Technology, Wuhan 430070, China;*
[2]*School of Power Engineering, Naval University of Engineering, Wuhan 430033, China;*
[3]*Hubei Collaborative Innovation Center for Advanced Organic Chemical Materials, Key Laboratory for the Synthesis and Application of Organic Functional Molecules of Ministry of Education, College of Chemistry and Chemical Engineering, Hubei University, Wuhan 430062, China*

Received February 23, 2022; accepted May 20, 2022; published online July 20, 2022

Carbon supported metal catalysts have received considerable interest due to their widespread applications in heterogeneous catalysis. However, the controllable synthesis of carbon support with defined morphology and composition still represents great challenging. Herein, we reported the synthesis of a well-defined hierarchically nanosized H-ZrO_2/NC (nitrogen-doped carbon) network *via* an inheritable carbonization strategy. When immobilizing the palladium clusters into the support, the N-doped sites and oxygen vacancy of the carbon composite can effectively stabilize and activate Pd through strong metal-support interaction which was also confirmed by density functional theory (DFT) calculations. Moreover, the hierarchically nanosized network can contribute to the exposure of active sites and facilitate the mass transfer during the catalytic process. As a result, benefiting from the hierarchical structure, composition and hydrolytic nature, Pd@H-ZrO_2/NC exhibited excellent catalytic activity and stability towards the hydrogenation of furfural in mild reaction conditions, as well as good universality toward the hydrogenation of a series of unsaturated hydrocarbons.

hierarchical carbon, nanosized networks, composites, metal-support interaction, catalytic hydrogenation

Citation: Pu C, Li RD, Chang GG, Chen MJ, Yao Y, Li JS, Zhao B, Wu L, Zhang YX, Yang XY. Hierarchical ZrO_2@N-doped carbon nano-networks anchored ultrafine Pd nanoparticles for highly efficient catalytic hydrogenation. *Sci China Chem*, 2022, 65: 1661–1669, https://doi.org/10.1007/s11426-022-1288-0

1 Introduction

Metal nanoparticles (MNPs) with small particle sizes have received attracting interest due to their crucial role in the catalytic domain [1–7]. Unfortunately, there exists a trade-off between the catalytic activity and stability of small-sized NPs since they are thermodynamically unstable and prone to aggregate owing to their high surface energy. Immobilizing the MNPs on the surface of appropriate support has been recognized as a prospective method to simultaneously stabilize and activate the MNPs, whose performance largely depends on the structure and composition of the supports [8–17]. Among various supports, carbon-based materials are widely employed mainly due to their large surface area and acid-alkali resistance [18–22]. However, the vast micro-

†These authors contributed equally to this work.
*Corresponding authors (email: changgang2016@whut.edu.cn; zhangyuexing@sdu.edu.cn; xyyang@seas.harvard.edu)

porous regime, inert chemical structure and amorphous morphology of traditionally porous carbons are not beneficial for the diffusion of substrate molecules, and suffer from aggregation and leach of active sites due to the weak interaction between the MNPs and carbon supports.

To date, numerous efforts like surface modification of the carbon framework (regulating the electronic structure) *via* the doping of heteroatoms (*e.g.*, N, P, or S) [23–28], or the construction of carbon composites [29–34] (*e.g.*, heterostructure with metallic oxides) have been devoted to enhancing the interactions between the carbon support and the MNPs, which in turn mediates their catalytic performance. Particularly, in terms of the metal-support interaction, the metallic oxides (*e.g.*, TiO_2, ZrO_2) usually with abundant oxygen-vacancies are frequently used as supports because of their high mechanical strength and strong metal-support interaction, which can effectively anchor the MNPs [35–41]. However, the significantly lower surface areas of metallic oxide itself restrict the exposure of active sites and the transportation of substrate molecules. Although downsizing the oxide supports is an effective strategy to increase the surface area-to-volume, the NPs usually face problems of poor thermal and chemical stability. In this regard, we speculate that the integration of nanosized oxide supports with the highly porous carbon, by combining both of the advantages of carbon materials and metal oxides might be an effective method to settle the above deficiencies. On the one hand, using the porous carbon matrix to assist the directed attachments of nanosized oxide NPs and disperse them, meanwhile greatly promote molecular accessibility. On the other hand, the incorporated metal oxides component can in turn meditate the inert nature of the carbon matrix and help to stabilize and activate the MNPs.

Traditionally, carbon-based materials are prepared by the carbonization of organic precursors usually through nanocasting or hard/soft-templating methods [42–44]. However, the chemical compositions and morphology of the resultants are still hard to control, moreover, the direct synthesis of the carbon@metal oxide heterostructures with sophisticated three-dimensional nanostructures still represents grand challenges. Recently, by virtue of their delicate crystalline structure and versatile composition, metal-organic frameworks (MOFs) [45–51] are deemed as promising sacrificial templates to fabricate highly porous carbon or composites with various controlled morphologies and compositions *via* inheritable carbonization strategy [52–58]. Pyrolysis of MOFs can not only obtain the linker-derived heteroatom doping of the carbon matrix to disperse and anchor the MNPs, but also brings in-situ derived metal oxides to enhance the interaction between MNPs and supports. Nevertheless, currently fabricated carbon composites through the pyrolysis of MOFs are mostly bulky size, nanosized carbon networks with a hierarchically porous structure that exhibiting huge advantages on the exposure of active sites and mass transportation are highly desired but usually require the help of specific instruments such as electrospinning setups [59–62].

Bearing the above considerations in mind, first of all, we fabricated a hierarchically amino-functionalized nanosized (~40 nm) UiO-66 (Zr) (H-UiO-66-NH_2, UiO for University of Oslo) network *via* a modified synthetic system referring to our previous methods [63]. Secondly, by direct pyrolysis of H-UiO-66-NH_2 precursor, a well-defined nanosized nitrogen-doped carbon network with hierarchical ZrO_2 micro-/mesoporosity and compositions (H-ZrO_2/NC) was successfully obtained. By introducing guest palladium (Pd) clusters into the support, N-doped sites and oxygen vacancy of ZrO_2 of the carbon composite can effectively stabilize and activate the Pd metal through the strong metal-support interaction. As a result, benefiting from the hierarchical porous structure, composition and hydrolytic nature, the resultant Pd@H-ZrO_2/NC exhibited excellent catalytic activity with complete conversion and selectivity towards the hydrogenation of furfural to furfuryl, as well as good universality toward a series of hydrogenation of unsaturated hydrocarbons. Remarkably, the catalytic activity was largely retained and the structure was maintained even after successive five cycles.

2 Experimental

2.1 Experimental materials

All chemicals were used as received without further purification. 2-Amino terephthalic acid (H_2BDC-NH_2, 99%), zirconium chloride ($ZrCl_4$, 98%), acetic acid (HAc, 99.8%), palladium(II) nitrate dihydrate ($Pd(NO_3)_2{\cdot}2H_2O$, 39.0%) were purchased by Shanghai Macklin Biochemical Co., Ltd. (China). The ethyl acetate (AR, 99.5%), hydrofluoric acid (HF, 40%), *N*,*N*-dimethylformamide (DMF, 99.9%) other organic solvents were obtained from Sinopharm Chemical Reagent Co. Benzaldehyde (AR, ≥98%), furfural (AR, 99%), decane (GC, 99%), 4-hydroxy benzaldehyde (AR, 98%), *p*-methyl benzaldehyde (98%), *p*-anisaldehyde (98%), vanillin (99%) and other unsaturated hydrocarbons were purchased from Aladdin Industrial Co. (China). Deionized water was used throughout this study.

2.2 Catalyst characterizations

The crystallinity and phase of the catalysts were characterized by the powder X-ray diffraction (XRD) patterns recorded on an X-ray diffractometer with Cu Kα radiation (D8 Advance, Bruker, λ=1.54059 Å). The thermostability of catalysts was measured by thermogravimetric analysis (TGA, DSC1) under air and Ar. Raman spectra were obtained using a Raman spectrometer (InVia, England) under the excitation of a 532 nm laser. The N_2 sorption isotherms

were measured at 77 K using an automatic volumetric adsorption analyzer Tristar II 3020. The size and surface morphology of catalysts observation were imaged with a field emission scanning electron microscope (FESEM, S-4800, HITACHI) and a transmission electron microscope (TEM, JEOL-2100F). The high angle annular dark field (HAADF) and energy-dispersive X-ray spectroscopy (EDS) elemental mapping images were carried out on an EDAX Genesis (USA). X-ray photoelectron spectroscopy (XPS) measurements were recorded on a PHI Quantera II, (ULVAC-PHI, Japan) for chemical composition analysis, all binding energies were calibrated to the C1s peak at 284.8 eV. Electron paramagnetic resonance (EPR) measurements were performed at the X-band using a JEOL FA 2000 spectrometer (Japan). The content of Pd was separately measured by inductively coupled plasma-atomic emission spectroscopy (ICP-AES, Prodigy7, Teledyne Leeman Labs, USA).

2.3 Catalyst preparations

2.3.1 Preparation of H-UiO-66-NH_2

In a typical procedure according to our previously reported methods [63], $ZrCl_4$ (0.7 mmol) and $H_2BDC\text{-}NH_2$ (0.7 mmol) were dispersed into a mixed solution of DMF/HAc/H_2O (18:1:3, *v*/*v*/*v*) in 50 mL Teflon-lined and then placed into stainless steel autoclave at 120 °C for 24 h. The as-obtained product was centrifuged and washed with deionized water and methanol three times when it cooled to room temperature. Subsequently, it was immersed into methanol for 24 h to purify and separated with centrifuge to obtain light yellow powders, named as H-UiO-66-NH_2. Finally, the as-prepared H-UiO-66-NH_2 was dried under vacuum at 100 °C for further use. The bulky amino-functionalized UiO-66 (Zr) (B-UiO-66-NH_2) was synthesized by the same method but with a DMF/HAc (18:1, *v*/*v*) solution of $ZrCl_4$ (0.7 mmol) and $H_2BDC\text{-}NH_2$ (0.7 mmol).

2.3.2 Preparation of hierarchically nanosized H-ZrO_2/NC-X and its contrasts

The above obtained H-UiO-66-NH_2 was placed in a tube furnace and then heated to 300 °C with a heating rate of 2 °C/min for keeping 2 h under the protection of Ar atmosphere. The calcination temperature was further raised to the set temperature (400, 500, 600, 700, 800 °C) with a heating rate of 5 °C/min for keeping 1 h under the protection of Ar atmosphere. The obtained powders were denoted as H-ZrO_2/NC-X (X=400, 500, 600, 70, 800 °C). The H-ZrO_2/NC-500 was suspended in an HF aqueous solution for 2 h and washed with deionized water, then the resulted black powders (named NC) were collected by centrifugation and finally dried under vacuum. The H-ZrO_2/NC-500 was calcinated at 600 °C in air atmosphere and gained gray powders (named ZrO_2). The B-ZrO_2/NC was synthesized by using B-UiO-66-NH_2 as precursors and directly carbonized at 500 °C.

2.3.3 Preparation of Pd@H-ZrO_2/NC and its contrast catalyst

Pd@H-ZrO_2/NC was synthesized by the wet impregnation method. 50 mg of H-ZrO_2/NC-500 was dispersed into 1 mL of deionized water, to which, 200 μL palladium nitrate solution with certain concentration (1.0 wt%, 3.0 wt%, 5.0 wt%) was added under stirring. After stirring for 12 h, the black solid was obtained directly vacuum dried at 70 °C, which was finally reduced in a tube furnace by passing 10% H_2/Ar as a reducing agent and heated to 200 °C at a rate of 5 °C/min for 3 h. ICP-AES results reveal that the Pd loading amount in Pd@H-ZrO_2/NC was 0.85 wt%, 2.48 wt%, and 4.12 wt%, respectively. For comparison, the same method was also applied to the synthesis of Pd@B-ZrO_2/NC, Pd@NC, and Pd@ZrO_2.

2.4 Density functional theory (DFT) calculations

All models were built using the Materials Visualizer interface of BIOVIA Materials Studio 2017 (17.1), and structural optimization and energy calculations were performed using the Dmol^3 module under BIOVIA Material Studio 2017 software. The generalized gradient approximation of Perdew-Burke-Ernzerh was used as the exchange correlation functional in the Kohn-Sham equation, and the effective core potentials were used to process the atomic orbitals and their electrons. The calculated atomic orbitals used the DND (version 3.5) basis set. The optimized graphene crystal was used to construct a carbon surface model (C), and on this basis, nitrogen atoms were used to replace carbon atoms to construct N-doped carbon surface model (NC). The optimized ZrO_2 crystal was used to construct the ZrO_2 (001) surface model (ZrO_2). an optimized Zr_8O_{16} cluster was placed on NC to build the composite material for modeling ZrO_2/NC. Pd atom was then put on different sites of C, NC, ZrO_2, and ZrO_2/NC. The most stable Pd adsorption models were named Pd@C, Pd@NC, Pd@ZrO_2, and Pd@ZrO_2/NC, respectively. The convergence criteria for structural optimization were set to: (a) 2×10^{-3} Hartree energy tolerance; (b) 1×10^{-5} Hartree SCF tolerance; (c) 5×10^{-3} Å maximum displacement tolerance; and (d) 4×10^{-3} Hartree/Å maximum force tolerance. The adsorption energy of Pd (defined as $E_{ad}=E_{syst}-E_{Pd}-E_{sys\text{-}withoutPd}$) and charge density difference analysis ($\rho_{ad}=\rho_{syst}-\rho_{Pd}-\rho_{sys\text{-}withoutPd}$) were then performed based on the optimized geometries, for which the energy convergence standard for single point energy calculation was set as 1×10^{-6} Hartree.

2.5 Catalytic reaction

Aqueous-phase hydrogenation of furfural was performed in a

25 mL stainless steel autoclave equipped with a mechanical stirrer, a pressure gauge and an automatic temperature control apparatus. Typically, catalyst (15 mg) and furfural (0.8 mmol) were dispersed in 5 mL deionized water. Then, the autoclave was sealed, purged six times with H_2 followed by pressurizing with 0.2 MPa H_2 and heating to a target temperature with mechanical stirring at 500 r/min. After finished, the autoclave was cooled down quickly with cold water and the products were extracted by ethyl acetate, and the catalyst could be recovered by filtration and washed several times with deionized water and ethanol, which was finally dried at 100 °C overnight. The products and substrates were analyzed by gas chromatography equipped with a HP-5 capillary column using decane as an internal standard. Quantitative analysis of products was done by interpolation calibration, using standard solutions of substrates and products.

3 Results and discussion

The fabrication process of hierarchically nanosized H-ZrO_2/NC network and contrastive bulky B-ZrO_2/NC particles *via* inheritable carbonization strategy are illustrated in Scheme 1. Of note, according to our previous report [63], the introduction of water during the solvothermal synthesis of UiO-66-NH_2 is essential to ensure the nanosized hierarchical network because of the accelerated nucleation process induced by water. After direct carbonization under relatively high temperature, the hierarchically nanosized H-ZrO_2/NC composite with a delicate network structure was intriguingly maintained. Moreover, for comparison, the individual NC (H-ZrO_2/NC treated by HF acid immersing) and ZrO_2 (H-ZrO_2/NC treated by calcination in air atmosphere) were also fabricated, respectively. By loading Pd sites into the support, the doped N sites and oxygen vacancy within H-ZrO_2/NC can be effectively used to stabilize and activate the Pd NPs through the strong metal-support interaction, while the hierarchically nanosized network can endow the H-ZrO_2/NC with huge advantages on the exposure of active sites and mass transportation.

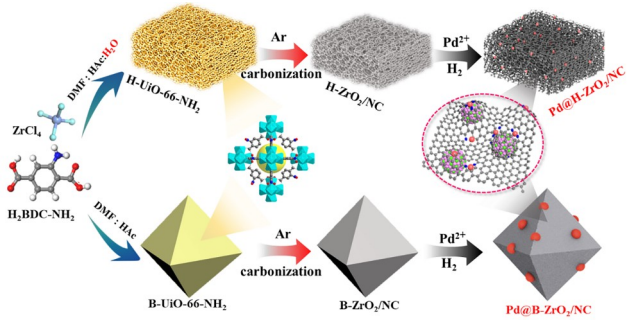

Scheme 1 The illustration of the stepwise synthesis process for Pd@H-ZrO_2/NC and contrastive Pd@B-ZrO_2/NC (color online).

3.1 Characterization of structural properties

The powder XRD patterns of H-UiO-66-NH_2 synthesized under water system were almost identical to that of calculated B-UiO-66-NH_2 except for the slightly broadened diffraction peaks at 7.4° and 8.5° (Figure S1a, Supporting Information online), indicating the nanosize reduction and the decrease of crystallinity degree of B-UiO-66-NH_2 [63]. The thermostability of H-UiO-66-NH_2 was measured by TGA in Ar and air (Figure S2). As shown in Figure S2, the obvious weight-loss temperature of H-UiO-66-NH_2 is around 350 °C, which can be attributed to the thermal degradation of frameworks. Thus, the pyrolysis temperature from 400 to 800 °C was chosen. The H-UiO-66-NH_2 was then directly employed as a sacrificed template to fabricate hierarchical carbon composites by calcination under various temperatures from 400 to 800 °C, and the XRD patterns of derived H-ZrO_2/NC-X (X=400–800 °C) were shown in Figure S1b. All the samples except for H-ZrO_2/NC-400 displayed characteristic diffraction peaks at 2θ=30.2°, 35.0°, 50.4° and 60.0°, which were indexed as the reflections of the typical tetragonal ZrO_2 (t-ZrO_2) (100), (110), (112) and (211) planes, respectively. No obvious characteristic peaks of ZrO_2 observed for the H-ZrO_2/NC-400 were probably ascribed to the low carbonization temperature, which was not high enough to form highly crystallized ZrO_2. Besides, the H-ZrO_2/NC-800 showed an additional weak peak at 2θ=28.0° belonged to the monoclinic ZrO_2 (m-ZrO_2) (−111) plane, implying the phase evolution from t-ZrO_2 to m-ZrO_2 along with the increase of temperature [64]. Figure 1a shows the XRD patterns of hierarchical H-ZrO_2/NC composite, bulky B-ZrO_2/NC, individual NC and ZrO_2 (unless otherwise stated, the pyrolysis temperature was fixed at 500 °C). The broad peak of NC at about 24° can be identified as amorphous carbon derived from the carbonization of organic frame-

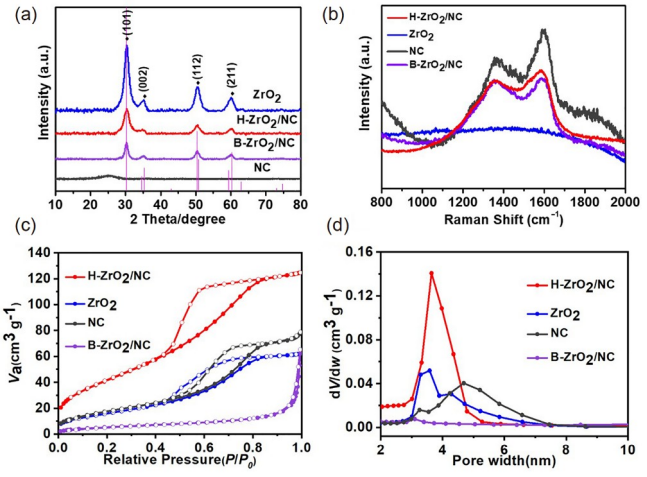

Figure 1 (a) XRD patterns, (b) Raman spectra, (c) N_2 adsorption-desorption isotherms, and (d) the corresponding pore size distribution curves of H-ZrO_2/NC, ZrO_2, NC, and B-ZrO_2/NC (color online).

works, and disappearance of any ZrO_2 characteristic peaks indicated that the ZrO_2 component had been successfully etched by acid treatment. Generally, the link-derived N-doped carbon can generate a large number of topological defects, and the graphitization degree can be evaluated with the intensity ratio of the D and G bands (I_D/I_G) at approximately 1,360 and 1,594 cm^{-1} in the Raman spectra (Figure 1b). The absence of D and G peaks for individual ZrO_2 indicated that the link-derived N-doped carbon was almost removed by calcination at air ambient, and the I_D/I_G values of H-ZrO_2/NC, B-ZrO_2/NC, and NC were calculated to be 0.82, 0.97, and 0.89, respectively. The lowest I_D/I_G values imply that the H-ZrO_2/NC nanocomposites possessed high graphitization degree, which may endow H-ZrO_2/NC with good dispersion in the aqueous solution [65].

The hierarchically porous networks of H-UiO-66-NH_2 and derived H-ZrO_2/NC-X were confirmed by the N_2 sorption isotherms (Figure S3a, b). Obviously, H-UiO-66-NH_2 showed a typical IV isotherm with a H_3-type hysteresis, indicating the hierarchically micro-/mesoporous structure induced by water, while for bulky B-UiO-66-NH_2, no hysteresis loop was observed. After carbonization, all samples of H-ZrO_2/NC-X also displayed typical IV isotherms with H_3-type hysteresis, indicating the possession of mesoporous structure inherited from H-UiO-66-NH_2. For comparison, the N_2 adsorption-desorption isotherms and pore size distribution curves of H-ZrO_2/NC, B-ZrO_2/NC, ZrO_2, and NC were shown in Figure 1c, d. Apparently, the curves of H-ZrO_2/NC, ZrO_2, and NC exhibited a pronounced hysteresis loop, also revealing the typical mesoporous character, but the surface areas were largely decreased from 177.0 m^2/g to 65.3 and 58.9 m^2/g when the ZrO_2 and NC were eliminated, respectively. Specific texture properties of all samples were summarized in Table S1 (Supporting Information online). In contrast, no hysteresis loop was observed for B-ZrO_2/NC, suggesting its microporous structure with significantly lower porosity. In addition, the pore size distribution curves also confirmed the wide pore size distribution of mesoporous (Figure 1d). For comparison, almost no surface areas and mesopore of B-ZrO_2/NC were observed. The large specific surface area and mesoporous size will contribute to the exposure of active sites and the mass transport of substrate molecules.

3.2 Characterization of morphology structure

The surface morphology of samples was characterized by scanning electron microscopy (SEM). As shown in Figure 2, the regular B-UiO-66-NH_2 precursor showed a relatively uniform octahedral morphology with a diameter of 150–200 nm (Figure 2a), while H-UiO-66-NH_2 synthesized with the addition of water exhibited significantly decreased particle size (~40 nm), which were further aggregated into a hierarchically interlaced network morphology (Figure 2b). When mild pyrolysis temperature (<800 °C) was employed, the carbonized H-ZrO_2/NC-X composites well inherited the hierarchically porous morphology of nanosized H-UiO-66-NH_2 but with slightly decreased particle size (~20 nm) due to the framework contraction. However, when higher pyrolysis temperature (800 °C) was employed, the hierarchically nanosized network was broken due to tempestuous fusion (Figure 2c and Figure S4). Besides, the morphology features of contrast samples were also shown in Figure S5. Note that the nanosized carbon networks with a hierarchically porous structure can exhibit intriguing advantages on the exposure of active sites and mass transportation. Transmission electron microscopy (TEM) was further performed to investigate the multiple compositions of the Pd@H-ZrO_2/NC heterostructure and the distribution of Pd NPs. The morphology and microstructure of the Pd@H-ZrO_2/NC catalyst were shown in Figure 2d, which confirmed the hierarchically nanosized network structure.

The averaged particle size of H-ZrO_2/NC was about 20 nm, and the pore size of the inter-aggregated network was about 4 nm, which was in accord with SEM and the results of the pore size distribution (Figure 2c and Figure S3d). From the high-resolution TEM (HRTEM) results of Pd@H-ZrO_2/NC (Figure 2e), the lattice spacing of 0.22 nm corresponding

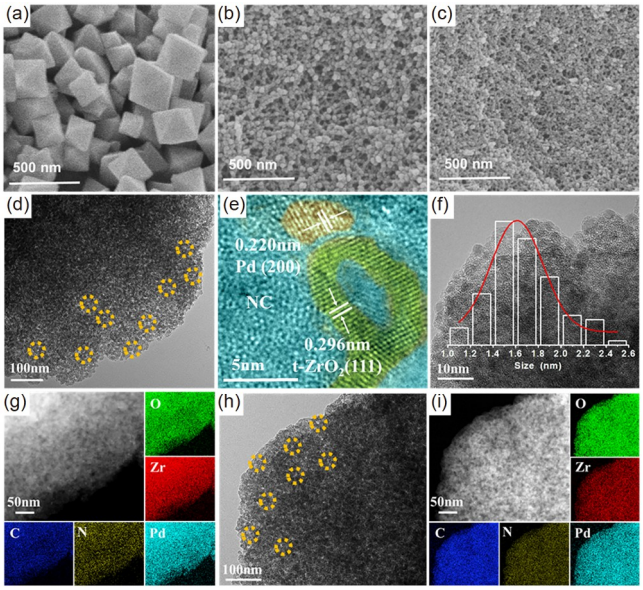

Figure 2 The FESEM images of (a) B-UiO-66-NH_2 (Zr), (b) H-UiO-66-NH_2 (Zr), and (c) H-ZrO_2/NC; (d) the TEM image of Pd@H-ZrO_2/NC (the yellow dotted circle represents pore between H-ZrO_2/NC); (e) the magnified HRTEM images of Pd@H-ZrO_2/NC (the inset are lattice spacing of the Pd nanoparticle (0.220 nm, red area) and ZrO_2 (0.296 nm, green area) corresponding to the Pd (200) and ZrO_2 (111) interplanar spacings); (f) the HRTEM image of Pd@H-ZrO_2/NC and corresponding size distribution of Pd NPs, (g) the high angle annular dark field (HADDF)-STEM and EDS mapping (C, N, Pd, Zr, O) images of Pd@H-ZrO_2/NC; (h) the TEM image and (i) HADDF-STEM and EDS mapping (C, N, Pd, Zr, O) images of Pd@H-ZrO_2/NC after five recycles (color online).

to the (111) plane of Pd NPs (red region), which was separately surrounded by node-derived ZrO_2 (d_{111}=0.296 nm, green region) nanocrystallites and linker-derived amorphous N-doped carbon (blue region), demonstrating the formation of multiple compositions of the Pd@H-ZrO_2/NC heterostructure. In addition, Figure 2f showed that Pd NPs were highly dispersed on H-ZrO_2/NC with an average particle size of 1.5 nm, and uniform distribution of Pd, C, N, O, and Zr were recorded by HAADF-STEM and EDS (Figure 2g). For comparison, the morphology of Pd@B-ZrO_2/NC was octahedral structure (150–200 nm) without interparticle mesopore. The Pd NPs were well dispersed in B-ZrO_2/NC, however, the average size of Pd NPs (2.5 nm) was larger than that of Pd@H-ZrO_2/NC (1.5 nm) (Figure S6).

3.3 Characterization of XPS and DFT calculations

To investigate the metal-support interaction between Pd NPs and H-ZrO_2/NC, the hierarchical Pd@H-ZrO_2/NC composite was examined by XPS. According to the survey scan (Figure S7a), we can confirm the co-existence of C, O, N, Zr, and Pd elements in the Pd@H-ZrO_2/NC catalysts. The N 1s spectra of Pd@H-ZrO_2/NC and H-ZrO_2/NC could be resolved into four types of N species with the domination of pyrrolic-N, graphitic-N, and pyridinic-N at 400.6, 400.0, and 398.6 eV (Figure S7b), respectively, which indicated that the N atoms were transformed into a π-conjugated system during high-temperature carbonization. In the high-resolution Zr 3d XPS spectrum of Pd@H-ZrO_2/NC, the binding energies at 182.3 and 184.7 eV corresponded to the Zr $3d_{5/2}$ and Zr $3d_{3/2}$ orbitals, respectively (Figure 3a), which shifted to a higher level (about 0.3 eV) compared to H-ZrO_2/NC that without Pd loading. Meanwhile, for the Pd 3d XPS spectrum of Pd@H-ZrO_2/NC (Figure 3b), two peaks centered at binding energies of 335.8 and 341.1 eV could be attributed to the Pd $3d_{5/2}$ and Pd $3d_{3/2}$ peak of Pd NPs, which shifted to relatively lower binding energy compared to Pd/NC without ZrO_2, revealing the strong electronic interactions within the multivariate composites. The strong interference peaks at 333.1 and 346.7 eV are ascribed to the Zr $3p_{3/2}$ and Zr $3p_{1/2}$ signal. In addition, the existence of abundant oxygen vacancies of Pd@H-ZrO_2/NC as identified by EPR spectroscopy (Figure 3c), which showed a typical symmetrical signal at a *g* value of 1.999 could also effectively anchor the Pd sites. To further verify this interaction between Pd species and different supports, DFT calculations were performed with the Dmol^3 program. Figure 3d–k showed the finally optimized geometries and the charge density difference stereograms of Pd binding on pure carbon matrix (C), N-doped carbon (NC), ZrO_2 and ZrO_2/NC surfaces, respectively. The calculated Pd adsorption energies of Pd@ZrO_2/NC were much higher (−3.44 eV) than those on pure carbon (−1.85 eV), individual Pd@NC (−2.13 eV) and Pd@ZrO_2 (−2.25 eV), signifying

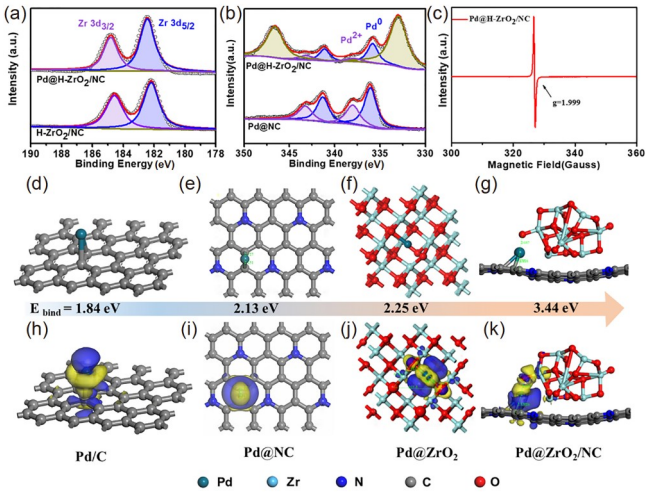

Figure 3 (a) The Zr 3d XPS images of Pd@H-ZrO_2/NC and H-ZrO_2/NC; (b) the Pd 3d XPS images of Pd@H-ZrO_2/NC, Pd@NC; (c) EPR of Pd@H-ZrO_2/NC; the interaction force between Pd and the support can be demonstrated by DFT using Dmol^3. Optimized structure of Pd adsorbed on pure carbon (d, h), N-doped carbon (e, i), ZrO_2 (f, j), and ZrO_2/NC (g, k) and their charge density difference analysis accordingly (blue: density gain, yellow: density loss) (color online).

stronger interaction between Pd and ZrO_2/NC than those on C, NC, and ZrO_2. Besides, the charge density difference stereograms shown the electron transfer state between the Pd atoms and supports, also revealed the highest electron density around Pd atoms in the Pd@ZrO_2/NC. The highest adsorption energy and electron delocalization compared to other individual components confirm the strong interaction between Pd and ZrO_2/NC which will contribute to the anchor and activation of Pd sites.

3.4 Catalytic performance

Motivated by the integrated advantages of the hierarchically nanosized network, multiple compositions and ultrafine Pd NPs, the catalytic hydrogenation performance of Pd@H-ZrO_2/NC was evaluated, of which, the aqueous hydrogenation of biomass-derived furfural (FAL) was selected as a model reaction. The optimal Pd loading amount was investigated for Pd@H-ZrO_2/NC, showing excellent catalytic performance with conversions (>99.0%) and selectivity (100%) when the loading amount reached 2.48 wt% (measured by ICP-AES), which was selected as the relative optimal loadings for the following hydrogenation reaction (Figure S8a). Particularly intriguing is that, both the decoration of N atoms and the integrated ZrO_2 greatly improve the wettability of Pd@H-ZrO_2/NC in contrast to the hydrophobicity of commercial Pd/C catalyst. As can be seen from Figure 4a, Pd@H-ZrO_2/NC was well dispersed in the water layer (with 67.1° of contact angle) and the commercial Pd/C was dispersed in the oil layer (ethyl acetate, with 109.4° of contact angle), indicating the wettability of Pd@H-ZrO_2/NC

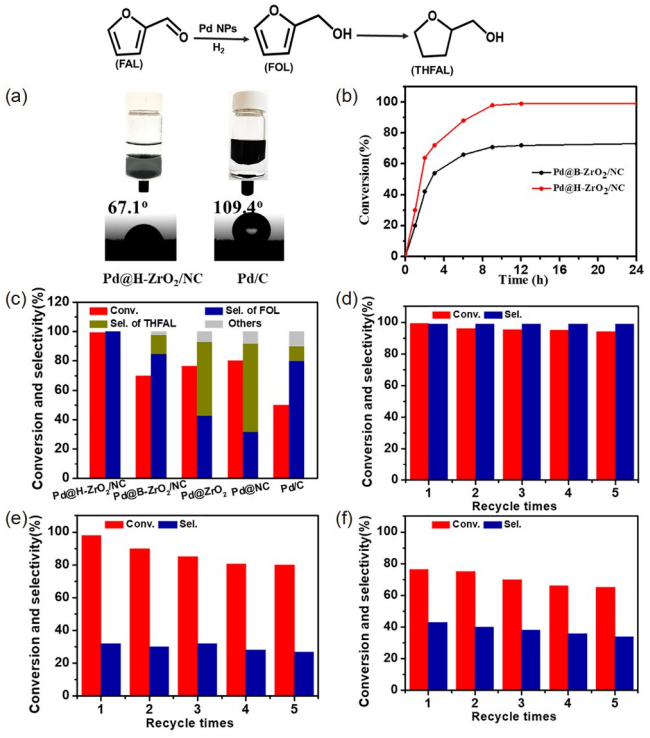

Figure 4 (a) The wettability (in water/ethyl acetate) and contact angle of Pd@H-ZrO_2/NC and commercial Pd/C; (b) the catalytic kinetic curve of Pd@H-ZrO_2/NC and Pd@B-ZrO_2/NC; (c) performance of different catalysts in the hydrogenation reaction of furfural; (d) recycling test of Pd@H-ZrO_2/NC; (e) recycling test of Pd@NC; (f) recycling test of Pd@ZrO_2. Reaction conditions: furfural (0.8 mmol), catalysts (15 mg), H_2O (5 mL), 0.3 MPa H_2, 80 °C,12 h (color online).

than commercial Pd/C. As shown in Figure 4b, the catalytic kinetics studies clearly showed that the Pd@H-ZrO_2/NC with hierarchically nanosized network exhibited relatively faster catalytic kinetics than the bulky Pd@B-ZrO_2/NC, demonstrating the structure advantages during mass transportation. Besides, Pd@H-ZrO_2/NC gave a furfuryl alcohol (FOL) selectivity as high as >99.0% with a complete conversion of FAL, outperforming the Pd NPs supported on individual Pd@ZrO_2, Pd@NC and Pd@B-ZrO_2/NC with the conversion of 76.5%, 80.1%, 70.3%, and selectivity of 43.2%, 32.5%, 85.0%, respectively (Figure 4c). Particularly, the hydrophobic commercial Pd/C only showed less than 50.0% conversion under the same reaction condition. More importantly, the catalytic stability of Pd@H-ZrO_2/NC, Pd@NC, and Pd@ZrO_2 towards the hydrogenation reaction of furfural was further investigated due to the importance for practical applications. As displayed in Figure 4d–f, Pd@H-ZrO_2/NC could be reused at least five times without loss of catalytic performance. And the representative TEM images and EDS mapping (C, N, Pd, Zr, O) images of Pd@H-ZrO_2/NC in Figure 2h, i showed that the well-ordered mesoporous structure and Pd NPs within Pd@H-ZrO_2/NC still maintained and no significant changes for the particle size of Pd NPs were observed after successive five reaction cycles. Besides, the XRD pattern of Pd@H-ZrO_2/NC after five catalytic cycles (Figure S9) still maintained the same as before, especially no identifiable peak for Pd NPs was observed, indicating its excellent structural stability. However, the catalytic performance of Pd@ZrO_2 and Pd@NC gradually decreased with recycling. The excellent catalytic activities and stability of Pd@H-ZrO_2/NC against other contrast samples (Pd@ZrO_2 and Pd@NC) unambiguously demonstrated the advantages of its hierarchical structure (mesoporous nanosized network) and ultrafine Pd NPs with abundant exposed active sites, as well as the possible synergistic effects among the multiple components to improve the activation and stabilization of active Pd NPs. Thus, based on the previous reports [66,67] and experimental results, a possible reaction pathway for the hydrogenation of furfural was proposed and shown in Scheme S1 (Supporting Information online).

In addition, the hierarchical Pd@H-ZrO_2/NC catalyst exhibited excellent catalytic performance toward the different investigated substrate molecules at moderate reactions condition in aqueous solution (Table 1). It could be found that both benzaldehyde (entry 1) and substituted benzaldehydes with electron-donating (*e.g.*, 4-OH, 4-CH_3, and 4-OCH_3, entries 2–5) or electron withdrawing (*e.g.*, 4-NC, 4-F, entries 6 and 7) were completely converted to corresponding hydrogenation alcohol, showing the excellent catalytic performance (>90.0% conversion with 100% selectivity) in aqueous solution. Note that the relatively lower selectivity for cinnamic aldehyde (entry 8) is due to the simultaneous hydrogenation of C=C groups. Such excellent catalytic performance could be attributed to the good wettability and the easy accessibility of Pd NPs within the hierarchical H-ZrO_2/NC which also can facilitate the mass transfer for the substrate molecules.

Table 1 Hydrogenation of unsaturated hydrocarbons over Pd@H-ZrO_2/NC [a)]

Entry	Substrate	Product	Conversion /%	Selectivity /%	TOF(TON)/h^{-1}
1	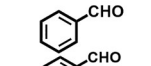	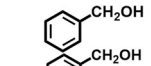	≥ 99.0	≥ 99.0	18.9(226.3)
2	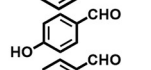	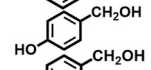	98.7	≥ 99.0	18.8(225.6)
3	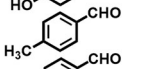	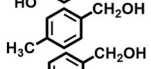	99.7	≥ 99.0	19.0(227.9)
4	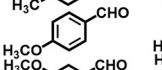	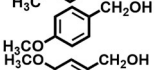	≥ 99.0	≥ 99.0	18.9(226.3)
5	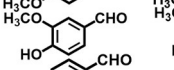	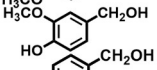	95.3	≥ 99.0	18.2(217.8)
6	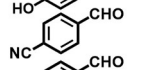	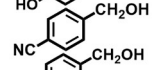	≥ 99.0	≥ 99.0	18.9(226.3)
7	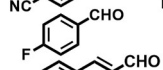	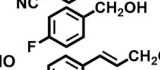	93.4	≥ 99.0	17.8(213.5)
8	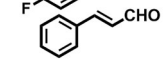	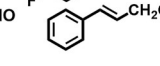	>99.0	70.0	18.9(226.3)

a) Reaction conditions: substrates (0.8 mmol), catalyst (15 mg), H_2O (5 mL), 0.3 MPa H_2, 80 °C, 12 h.

4 Conclusions

In summary, we have demonstrated the successful fabrication of a hierarchically nanosized (~20 nm) H-ZrO_2/NC network by direct pyrolysis of a hierarchically amino-functionalized H-UiO-66-NH_2 (Zr) simply synthesized in the water-added solvent system. The nanosized H-ZrO_2/NC networks showed an inheritable micro-/mesoporous structure and multiple chemical compositions, which were further utilized as support for active Pd sites. The XPS characterization and DFT calculations revealed that the N-doped sites and oxygen vacancy of ZrO_2 of the carbon composite could effectively stabilize and activate the Pd NPs through the strong metal-support interaction, which resulted in the formation of highly dispersed and ultrafine Pd NPs (~1.5 nm). Besides, both the decoration of N atoms and the integrated ZrO_2 greatly improved the wettability of Pd@H-ZrO_2/NC. When applying the hierarchical Pd@H-ZrO_2/NC composite to the water-phase hydrogenation of furfural, excellent catalytic activity with complete conversion (>99%) and selectivity (>99%) towards furfuryl was achieved, which outperformed the contrast bulky Pd@B-ZrO_2/NC, individual catalyst, and hydrophobic commercial Pd/C. More importantly, hierarchical Pd@H-ZrO_2/NC exhibited excellent catalytic performance toward the hydrogenation of a series of unsaturated hydrocarbons in the aqueous system, and the catalytic activity and the structural stability were still retained after successive five cycles. The remarkable catalytic performances of Pd@H-ZrO_2/NC are associated with its hierarchical nano-networks, ultrafine Pd NPs and hydrophilic nature. This work sheds light on their performance and structure advantages of hierarchically nanosized carbon networks for catalytic applications, which might open an avenue for developing highly efficient catalysts with hierarchically controlled structures and compositions.

Acknowledgements This work was supported by the National Natural Science Foundation of China (21706199, 51861135313), Rapid Response Bilateral Collaborative Funding of the Sino-German Centre for Research Promotion (C-0046), Guangdong Province International Scientific and Technological Cooperation Projects (2020A0505100036), the National 111 project (B20002), the Program for Changjiang Scholars and Innovative Research Team in University (IRT_15R52, PCSIRT), the International Science & Technology Cooperation Program of China (2015DFE52870), and The Young Top-notch Talent Cultivation Program of Hubei Province.

Conflict of interest The authors declare no conflict of interest.

Supporting information The supporting information is available online at http://chem.scichina.com and http://link.springer.com/journal/11426. The supporting materials are published as submitted, without typesetting or editing. The responsibility for scientific accuracy and content remains entirely with the authors.

1 Zhang L, Zhou M, Wang A, Zhang T. *Chem Rev*, 2020, 120: 683–733
2 Liu L, Corma A. *Chem Rev*, 2018, 118: 4981–5079
3 Yang Q, Xu Q, Jiang HL. *Chem Soc Rev*, 2017, 46: 4774–4808
4 Murdoch M, Waterhouse GIN, Nadeem MA, Metson JB, Keane MA, Howe RF, Llorca J, Idriss H. *Nat Chem*, 2011, 3: 489–492
5 Cure J, Mattson E, Cocq K, Assi H, Jensen S, Tan K, Catalano M, Yuan S, Wang H, Feng L, Zhang P, Kwon S, Veyan JF, Cabrera Y, Zhang G, Li J, Kim M, Zhou HC, Chabal YJ, Thonhauser T. *J Mater Chem A*, 2019, 7: 17536–17546
6 Wang N, Sun Q, Yu J. *Adv Mater*, 2019, 31: 1803966
7 Yang Q, Liu W, Wang B, Zhang W, Zeng X, Zhang C, Qin Y, Sun X, Wu T, Liu J, Huo F, Lu J. *Nat Commun*, 2017, 8: 14429
8 Gao C, Lyu F, Yin Y. *Chem Rev*, 2021, 121: 834–881
9 Nilsson Pingel T, Jørgensen M, Yankovich AB, Grönbeck H, Olsson E. *Nat Commun*, 2018, 9: 2722
10 Khan HA, Hao J, Farooq A. *Chem Eng J*, 2020, 397: 125489
11 Han B, Guo Y, Huang Y, Xi W, Xu J, Luo J, Qi H, Ren Y, Liu X, Qiao B, Zhang T. *Angew Chem Int Ed*, 2020, 59: 11824–11829
12 Bi F, Zhang X, Chen J, Yang Y, Wang Y. *Appl Catal B-Environ*, 2020, 269: 118767
13 Wang L, Wang L, Meng X, Xiao FS. *Adv Mater*, 2019, 31: 1901905
14 Lamme WS, van der Heijden O, Krans NA, Nöllen E, Mager N, Hermans S, Zečević J, de Jong KP. *J Catal*, 2019, 375: 448–455
15 Huang KX, Hua J, Chang GG, Li Z, Tian G, Chen MJ, Li JX, Ke SC, Yang XY, Chen B. *Small*, 2021, 17: 2002811
16 He L, Weniger F, Neumann H, Beller M. *Angew Chem Int Ed*, 2016, 55: 12582–12594
17 Li L, Li Z, Yang W, Huang Y, Huang G, Guan Q, Dong Y, Lu J, Yu SH, Jiang HL. *Chem*, 2021, 7: 686–698
18 Liu X, Dai L. *Nat Rev Mater*, 2016, 1: 16064
19 Yang W, Li X, Li Y, Zhu R, Pang H. *Adv Mater*, 2018, 31, 6: 1804740
20 Kaiser SK, Surin I, Amorós-Pérez A, Büchele S, Krumeich F, Clark AH, Román-Martínez MC, Lillo-Ródenas MA, Pérez-Ramírez J. *Nat Commun*, 2021, 12: 4016
21 Pu C, Zhang J, Chang G, Xiao Y, Ma X, Wu J, Luo T, Huang K, Ke S, Li J, Yang X. *Carbon*, 2020, 159: 451–460
22 Rao RG, Blume R, Hansen TW, Fuentes E, Dreyer K, Moldovan S, Ersen O, Hibbitts DD, Chabal YJ, Schlögl R, Tessonnier JP. *Nat Commun*, 2017, 8: 340
23 Wang H, Shao Y, Mei S, Lu Y, Zhang M, Sun JK, Matyjaszewski K, Antonietti M, Yuan J. *Chem Rev*, 2020, 120: 9363–9419
24 Yang W, Zhang S, Chen Q, Zhang C, Wei Y, Jiang H, Lin Y, Zhao M, He Q, Wang X, Du Y, Song L, Yang S, Nie A, Zou X, Gong Y. *Adv Mater*, 2020, 32: 2001167
25 Dong M, Wang X, Wu C. *Adv Funct Mater*, 2020, 30: 1908519
26 Jackson C, Smith GT, Inwood DW, Leach AS, Whalley PS, Callisti M, Polcar T, Russell AE, Levecque P, Kramer D. *Nat Commun*, 2017, 8: 15802
27 Wang B, Yue Y, Jin C, Lu J, Wang S, Yu L, Guo L, Li R, Hu ZT, Pan Z, Zhao J, Li X. *Appl Catal B-Environ*, 2020, 272: 118944
28 Wang R, Dong XY, Du J, Zhao JY, Zang SQ. *Adv Mater*, 2018, 30: 1703711
29 Liu C, Sun Q, Lin L, Wang J, Zhang C, Xia C, Bao T, Wan J, Huang R, Zou J, Yu C. *Nat Commun*, 2020, 11: 4971
30 Chai L, Pan J, Hu Y, Qian J, Hong M. *Small*, 2021, 17: 2100607
31 Xia C, Wang H, Kim JK, Wang J. *Adv Funct Mater*, 2021, 31: 2008247
32 Liu K, Qin R, Zheng N. *J Am Chem Soc*, 2021, 143: 4483–4499
33 Singh TI, Rajeshkhanna G, Pan UN, Kshetri T, Lin H, Kim NH, Lee JH. *Small*, 2021, 17: 2101312
34 Wang M, Xu Y, Peng CK, Chen SY, Lin YG, Hu Z, Sun L, Ding S, Pao CW, Shao Q, Huang X. *J Am Chem Soc*, 2021, 143: 16512–16518
35 van Deelen TW, Hernández Mejía C, de Jong KP. *Nat Catal*, 2019, 2: 955–970
36 Li Z, Chen Y, Ji S, Tang Y, Chen W, Li A, Zhao J, Xiong Y, Wu Y, Gong Y, Yao T, Liu W, Zheng L, Dong J, Wang Y, Zhuang Z, Xing W, He CT, Peng C, Cheong WC, Li Q, Zhang M, Chen Z, Fu N, Gao X, Zhu W, Wan J, Zhang J, Gu L, Wei S, Hu P, Luo J, Li J, Chen C, Peng Q, Duan X, Huang Y, Chen XM, Wang D, Li Y. *Nat Chem*,

2020, 12: 764–772
37 Ro I, Resasco J, Christopher P. *ACS Catal*, 2018, 8: 7368–7387
38 Parastaev A, Muravev V, Huertas Osta E, van Hoof AJF, Kimpel TF, Kosinov N, Hensen EJM. *Nat Catal*, 2020, 3: 526–533
39 Tan Q, Shu C, Abbott J, Zhao Q, Liu L, Qu T, Chen Y, Zhu H, Liu Y, Wu G. *ACS Catal*, 2019, 9: 6362–6371
40 Chen K, Li Y, Wang M, Wang Y, Cheng K, Zhang Q, Kang J, Wang Y. *Small*, 2021, 17: 2007527
41 Wang C, Kim J, Tang J, Kim M, Lim H, Malgras V, You J, Xu Q, Li J, Yamauchi Y. *Chem*, 2020, 6: 19–40
42 Jiao L, Zhang R, Wan G, Yang W, Wan X, Zhou H, Shui J, Yu SH, Jiang HL. *Nat Commun*, 2020, 11: 2831
43 Lee J, Kim J, Hyeon T. *Adv Mater*, 2006, 18: 2073–2094
44 Benzigar MR, Talapaneni SN, Joseph S, Ramadass K, Singh G, Scaranto J, Ravon U, Al-Bahily K, Vinu A. *Chem Soc Rev*, 2018, 47: 2680–2721
45 Cai G, Yan P, Zhang L, Zhou HC, Jiang HL. *Chem Rev*, 2021, 121: 12278–12326
46 Fang R, Dhakshinamoorthy A, Li Y, Garcia H. *Chem Soc Rev*, 2020, 49: 3638–3687
47 Ma XC, Pu C, Zhang YX, Chang GG, Tian G, Wu SM, Liu JW, Hu ZY, Wang LY, Yin YX, Janiak C, Yang XY. *Chem Eng J*, 2022, 429: 132128
48 Xiao YY, Liu XL, Chang GG, Pu C, Tian G, Wang LY, Liu JW, Ma XC, Yang XY, Chen B. *Nanoscale*, 2020, 12: 6250–6255
49 Chang GG, Ma XC, Zhang YX, Wang LY, Tian G, Liu JW, Wu J, Hu ZY, Yang XY, Chen B. *Adv Mater*, 2019, 31: 1904969
50 Ke S, Chang G, Hu Z, Tian G, Yang D, Ma X, Huang K, Li J, Yang X. *ACS Sustain Chem Eng*, 2020, 8: 966–976
51 Wu J, Chang GG, Peng YQ, Ma XC, Ke SC, Wu SM, Xiao YX, Tian G, Xia T, Yang XY. *Chem Commun*, 2020, 56: 6297–6300
52 Tang J, Yamauchi Y. *Nat Chem*, 2016, 8: 638–639
53 Dang S, Zhu QL, Xu Q. *Nat Rev Mater*, 2018, 3: 17075
54 Wang Q, Astruc D. *Chem Rev*, 2020, 120: 1438–1511
55 Huang A, Nie R, Zhang B, Pei Y, Chen M, Behera R, Yu J, Luan X, Hunter NT, Ke M, Huang W. *ChemCatChem*, 2020, 12: 602–608
56 Kong L, Zhu J, Shuang W, Bu XH. *Adv Energy Mater*, 2018, 8: 1801515
57 Hou CC, Zou L, Xu Q. *Adv Mater*, 2019, 31: 1904689
58 Xie X, Peng L, Yang H, Waterhouse GIN, Shang L, Zhang T. *Adv Mater*, 2021, 33: 2101038
59 Chen LF, Lu Y, Yu L, Lou XWD. *Energy Environ Sci*, 2017, 10: 1777–1783
60 Xue J, Wu T, Dai Y, Xia Y. *Chem Rev*, 2019, 119: 5298–5415
61 Su Q, Zeng S, Tang M, Zheng Z, Wang Z. *Energy Technol*, 2021, 9: 2100049
62 Park SK, Park JS, Kang YC. *J Mater Chem A*, 2018, 6: 1028–1036
63 Li J, Chang G, Tian G, Pu C, Huang K, Ke S, Janiak C, Yang X. *Adv Funct Mater*, 2021, 31: 2102868
64 Zhao Y, Zhou H, Chen W, Tong Y, Zhao C, Lin Y, Jiang Z, Zhang Q, Xue Z, Cheong WC, Jin B, Zhou F, Wang W, Chen M, Hong X, Dong J, Wei S, Li Y, Wu Y. *J Am Chem Soc*, 2019, 141: 10590–10594
65 Chen YZ, Cai G, Wang Y, Xu Q, Yu SH, Jiang HL. *Green Chem*, 2016, 18: 1212–1217
66 Mironenko RM, Belskaya OB, Talsi VP, Likholobov VA. *J Catal*, 2020, 389: 721–734
67 Zhao Z, Bababrik R, Xue W, Li Y, Briggs NM, Nguyen DT, Nguyen U, Crossley SP, Wang S, Wang B, Resasco DE. *Nat Catal*, 2019, 2: 431–436